Received 28 March 2025; Accepted 7 May 2025;
https://doi.org/10.48612/letters/2025-2-104-111

https://elibrary.ru/biesnw

Crystallography of the martensitic transformation in friction-stir processed 10% chromium martensitic steel

A. A. Kalinenko†[1], I. S. Nikitin[1], R. V. Mishnev[1,2], S. S. Malopheyev[1]

†kalinenko@bsuedu.ru

[1]Laboratory of Mechanical Properties of Nanoscale Materials and Superalloys, Belgorod National Research University, Belgorod 308015, Russia
[2]Wuhan University of Science and Technology, Wuhan 430081, Hubei, P. R. China

Abstract: In this study, the martensitic transformation that occurred in the friction-stir processed (FSPed) 10% Cr martensitic steel was studied. Due to the specific character of the FSP technique, the processed material undergoes very large plastic strains at an elevated temperature and a high strain rate. It is important to emphasize that material flow during FSP of martensitic steels usually occurs in the austenitic phase field. During subsequent cooling cycle, the processed material typically experiences martensitic transformation. It is expected that the heavily-deformed and fine-grained microstructure produced in the austenitic phase during FSP may exert an influence on the following martensitic transformation. Specifically, deviations from the "conventional" orientation relationship and selection of crystallographic variants are anticipated. To the best of authors' knowledge, this issue is still not studied well. Therefore, the present work aimed to shed some light on this phenomenon. To this end, the electron backscatter diffraction (EBSD) technique was applied to characterize the microstructure produced during FSP of 10% Cr creep-resistant steel. It was found that the evolved microstructure was indeed dominated by martensitic phase, though it also contained a minor fraction (≈0.1%) of retained austenite. It was also shown the orientation relationship between the martensite and austenite deviated from the "classical" Kurdjumov-Sachs (K-S) one and could be described in terms of a mixture of K-S and Nishiyama-Wasserman (N-W) relationships. This observation was attributed to the essential orientation spread within the prior austenite grains. Moreover, a pronounced variant selection was revealed in the martensitic phase. The reconstruction of the microstructure of high-temperature austenite had demonstrated that the latter observation was likely due to the pronounced grain refinement and development of a distinct B/-B {110}<112> simple shear texture occurring in the austenitic phase during FSP.

Keywords: martensitic steel, friction stir welding/processing, severe plastic deformation, electron backscatter diffraction, microstructure, martensitic transformation, orientation relationship, reconstruction of prior austenite grains

Acknowledgements: *This research was funded by the Russian Science Foundation, grant No. 24-79-00138, https://rscf.ru/en/project/24-79-00138/. The experimental work was performed using the equipment of the Research Equipment Sharing Center "Technology and Materials" at Belgorod National Research University.*

1. Introduction

Friction-stir welding/processing (FSW/P) is an innovative solid-state technology for joining metallic materials or modifying their microstructure. Since steels represent the structural materials that are most widely used in engineering, it is expected that the application of FSW/P technology for steels would be of great practical importance. As a result, intensive research is being focused in this area.

Given the relatively high-strength nature of steels, the application of FSW/P faces essential difficulties. Specifically, expensive welding tools are required for this purpose. These include ones fabricated from either boron nitride ceramics [1–4], or silicon nitride ceramics [5,6], or zirconium carbide ceramics [7], as well as the high-strength alloys based on tungsten [8–13] or nickel [12]. During FSW/P, an extensive abrasion of the welding tools [4,5] and the active oxidation of the welded/processed materials typically occur. In order to minimize these undesirable effects, it is recommended to apply protective tool coatings [8,9] and use shielding gases (e.g. argon) [5].

Usually, the peak temperature during FSW/P of steels lies in the austenitic phase field. Accordingly, the final microstructure originates from either martensitic [8,15–17] or bainitic [11,18] phase transformation that occurred during the cooling of the welded/processed material down to the ambient temperature. In some cases, however, material flow may also develop within the ferrite-austenite phase field, thus resulting in the ultrafine-grained ferrite-martensitic microstructure within the stir zone [8,19–24]. Such microstructures benefit from a good combination of strength and ductility [21,22]. Typically, the steels subjected to FSW/P exhibit excellent strength [14,25,26], good fatigue endurance [21], and satisfactory ductility [25].

Despite the above studies having provided valuable insight into the FSW/P of steels, fundamental aspects of the underlying microstructural processes are still not completely clear. It is expected that extremely large plastic strains inherent to the FSW/P process would result in a heavily-deformed and fine-grained structure and a distinct crystallographic texture in the austenite phase field. In turn, this may exert a substantial influence on the subsequent martensitic transformation. Specifically, a deviation from the "classical" orientation relationship(s) between the austenite and martensite as well as a selection of crystallographic variants is anticipated. Moreover, wear of the welding tool (which usually occurs during FSW/P of steels) and concomitant mechanical alloying of the stir zone material can also affect the structure of the processed material.

The present study was undertaken in order to evaluate the above hypothesis with the aim of broadening our understanding of martensitic transformations.

2. Materials and methods

The material used in the present study was 10% chromium martensitic steel, whose measured chemical composition is shown in Table 1. The chemical composition of the material was determined using a Foundry Master OE750 optical emission spectrometer and a METEK-300/600 nitrogen, hydrogen, and oxygen analyzer.

The material was produced by the vacuum induction melting. The cast ingot was homogenized at 1160°C and then forged into a strip with height 65 mm and width 140 mm with the final forging temperature being 850°C. Thereafter, it was normalized at 1060°C for 1 hour and finally tempered at 770°C for 3 hours, followed by air-cooling. The heat treatment procedures were carried out using an electric resistance furnace Nabertherm GmbH equipped with a temperature controller. Hereafter, this material condition was referred to as base material. The base material was sliced into a series of sheets of $70 \times 65 \times 3.4$ mm^3 in size using a Sodick electrical discharge machine for the subsequent FSP experiments.

The FSP trials were conducted using an AccuStir 1004 machine (General Tool Company) at the tool rotation rate of 1100 rpm and the tool travel speed of 25.4 mm/min. The welding tool was fabricated from a WC+10%Co (YL 10.2 grade) alloy and consisted of a flat shoulder of 12.2 mm in diameter and a hemispherical probe of 2.9 mm in length.

For microstructural observations and microhardness measurements, the processed material was sectioned perpendicular to the welding direction (WD). Then, the microstructural samples were mechanically polished in a conventional fashion with the final step involving the long-term (24 hours) vibratory polishing with commercial OP-S suspension.

Microstructural examinations were conducted using scanning electron microscopy (SEM), energy-dispersive X-ray spectroscopy (EDS), and electron backscatter diffraction (EBSD). The EBSD data were processed and analyzed using TSL OIM Analysis 8 software.

To assist the interpretation of microstructure distribution within the processed material, a microhardness map was measured from the entire FSPed zone. The Vickers microhardness data were collected using a Wolpert 402MVD microhardness tester by applying a load of 5 N, a dwell time of 10 s, and a step size of 0.5 mm.

3. Results

The microhardness map measured from the transverse cross-section of the processed material is shown in Fig. 1. The color code for the microhardness measurements is given in the bottom left corner. The fairly inhomogeneous distribution of the microhardness revealed in the map implied significant microstructural changes that occurred during FSP.

In the *base material zone* (i.e., the area that experienced neither deformation nor temperature influence), the average microhardness was measured to be about 230 HV. In the *stir zone* (i.e., the material that was stirred during FSP), a considerable hardening effect was observed. Depending on a particular location, the microhardness varied from 500 to 700 HV. The revealed hardening effect implied the martensitic transformation that presumably occurred during FSP [8,15–17].

It is also important to note that a transition region between the base material and stir zone exhibited a measurable material softening down to about 190–200 HV (Fig. 1). In the scientific literature, this phenomenon is typically attributed to the martensite tempering and the concomitant microstructural zone is referred to as the *heat-affected zone*.

Table 1. Chemical composition of the martensitic steel (in wt.%).

C	Si	Mn	Cr	Ni	Co	Mo	W	V	Nb	B	N	Al	Fe
0.1	0.07	0.11	9.74	0.16	2.9	0.68	1.9	0.2	0.05	0.008	0.003	0.01	bal.

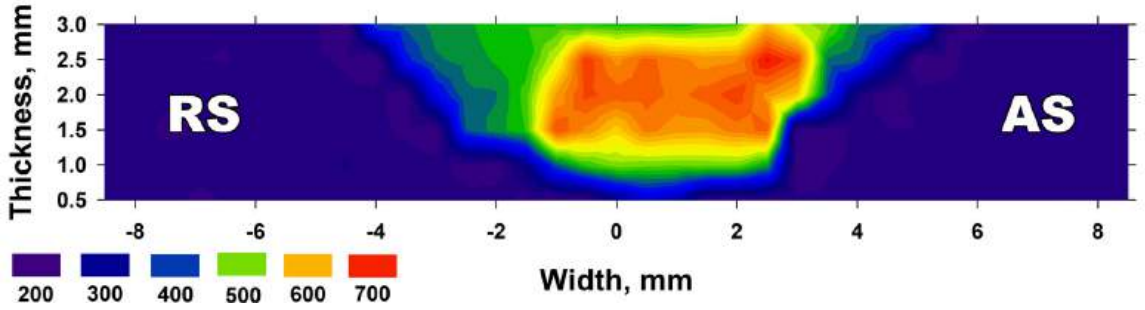

Fig. 1. (Color online) Microhardness map measured from the transverse cross-section of the friction-stir processed martensitic steel. RS and AS are retreating side and advancing side, respectively.

In order to reveal the possible origin of the microhardness scattering observed within the stir zone, the processed material was examined using back-scatter electron ("Z-contrast") imaging, as shown in Fig. 2a. It was found that the stir zone material contained a significant fraction of the bright-contrast particles that were arranged in a nearly concentric circle distribution. EDS measurements demonstrated that the particles were enriched by tungsten (Fig. 2b) and cobalt (Fig. 2c), i.e., constituent elements of the material of the welding tool. This observation presumably implies that the particles originated from wear of the welding tool during FSP, in agreement with extensive data in the scientific literature [4,5]. The inhomogeneous distribution of the tool debris within the stir zone explains microhardness scattering.

Remarkably, the tool debris also contained notable fractions of iron and chromium (Fig. 2c), i.e., constituent elements of the FSPed high-chromium steel. This suggests that the wear mechanism perhaps involved an intermetallic reaction between the welding tool and processed material, thus being a "chemical" wear in nature.

To examine the microstructure evolved within the stir zone, a series of EBSD maps was taken from its central section, with the typical example being shown in Fig. 3a. In this map, individual grains are colored according to their crystallographic orientations relative to the WD (the color code of the orientations is given in the upper right corner). In accordance with expectations, a typical martensitic structure was found that consisted of prior-austenite grains, martensite packets, and martensite blocks. Only a minor fraction (≈0.1%) of retained austenite was detected (Fig. 3b). Typically, the retained austenite was arranged as fine particles distributed along grain boundaries within the martensitic phase (Fig. 3b). It is also worth noting that an increased fraction of the retained austenite was observed in the vicinity of the tool debris (not shown).

In order to inspect the possible orientation relationship between the retained austenite and martensite, orientation data from the phases were arranged as a series of pole figures and compared with each other, as exemplified in Fig. 3c. It was surprisingly found that the orientation relationship between the austenite and martensite can be described in terms of both the Kurdjumov-Sachs (K-S) orientation relationship, i.e., $<111>_{\gamma} \| <110>_{\alpha'}$ and $\{110\}_{\gamma} \| \{111\}_{\alpha'}$ and the Nishiyama-Wasserman (N-W) orientation relationship, i.e., $<111>_{\gamma} \| <110>_{\alpha'}$ and $\{112\}_{\gamma} \| \{110\}_{\alpha'}$.

To provide a deeper insight into the orientation relationship, orientation data were taken from a single prior-austenite grain (an example is indicated by the dotted line in Fig. 3a). Then the data were arranged as a 100 pole figure (Fig. 4c) and compared with that expected for both the ideal K-S orientation relationship (Fig. 4a) and the ideal N-W orientation relationship (Fig. 4b). It was found that the distribution of the measured orientations in the 100 pole figure was circular rather than straight in appearance

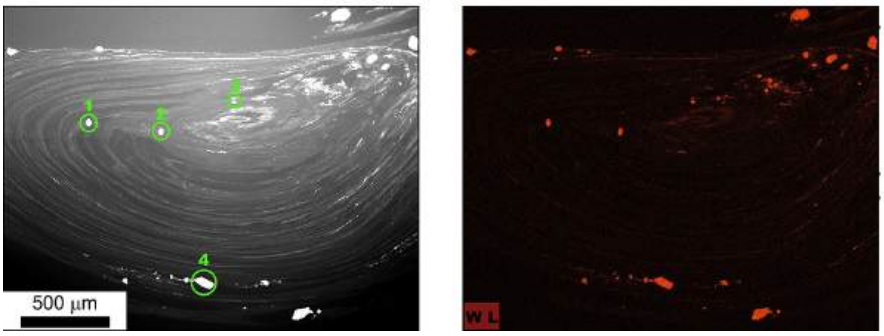

1		2	
Element	Weight, %	Element	Weight, %
Fe K	3.87	Cr K	1.97
Co K	11.31	Fe K	3.23
W L	84.82	Co K	10.62
		W L	84.18
3		**4**	
Cr	2.50	Cr	1.96
Fe K	7.93	Fe K	8.57
Co K	8.77	Co K	9.01
W L	80.80	W L	80.46

a b c

Fig. 2. (Color online) Macro-scale structure within the stir zone: backscatter-electron scanning-electron-microscopy (BSE-SEM) image (a), energy-dispersive X-ray spectroscopy (EDS) map (b), and chemical composition of the particles indicated by the green circles in Fig. 2a (c). In (b), the tungsten-rich areas are highlighted with red.

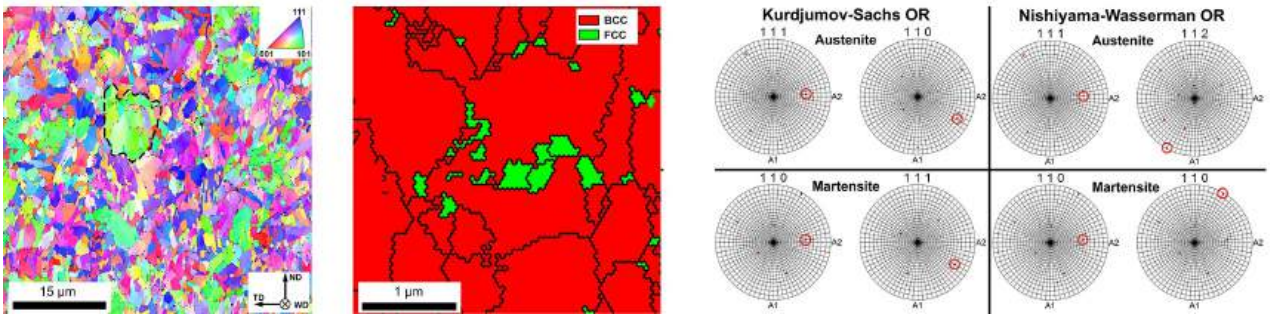

a b c

Fig. 3. (Color online) Typical microstructure within the central part of the stir zone: EBSD inverse-pole-figure map (color code triangle is given in the top right corner) (a), a selected portion of the EBSD phase map illustrating retained austenite (b), and pole figures showing the local orientation relationship between the retained austenite and the martensite (c). In (a), selected area exemplifies a prior-austenite grain. In (c), the closest related directions in the austenite and the martensite are circled. WD, TD, and ND are welding direction, transverse direction, and normal direction, respectively.

(Fig. 4c). This observation was interpreted as an evidence of the prevalence of the K-S orientation relationship.

On the other hand, it is important to emphasize that the measured orientations also exhibited a substantial orientation spread (Fig. 4c), thus perhaps reflecting the heavily-deformed nature of the prior-austenite grains. Given the relatively small orientation difference between the K-S and N-W relationships, the revealed orientation spread explains well the apparent controversy seen in Fig. 3c. Thus, to account for the orientation spread, a mixed orientation relationship (according to which the K-S and N-W relationships act simultaneously) may be used.

Attempting to provide an additional insight into the martensitic transformation, misorientation distribution was derived from EBSD data, as shown in Fig. 5a.

The misorientation-angle distribution in the martensitic phase (Fig. 5a) exhibited a pronounced low-angle maximum and a broad peak in the angular range of 50 – 60° (Fig. 5a). Moreover, the clustering of rotation axes near <111> and <110> poles was also observed, as shown in an insert in the upper section of (a). Such misorientation distributions are typically found in martensitic structures. Therefore, the misorientation measurements confirm the martensitic transformation occurred during the cooling of the material after FSP.

Due to the symmetry of crystal structures of the martensite and austenite phases, there are 24 possible variants that obey the K-S orientation relationship (listed in Table S1, Supplementary material) [29 – 31]. The theoretical misorientations between variant 1 (V1) and other martensite variants (V2 to V24), expected for the K-S orientation relationship, were summarized in the Table S2 [32].

In order to examine the possibility of the variant selection occurring during the martensitic transformation, the fraction of misorientations between martensitic variants according to the K-S orientation relationship were measured and summarized in Fig. 5b. Considering the limited accuracy of EBSD, the boundary fractions were measured within a tolerance of 5°. This resulted in overlapping of some intervariant boundaries, such as V3 and V5, V9 and V19, and V10 and V14 (Fig. 5b).

It is clear from Fig. 5b that the distribution is not uniform but exhibits a distinct crystallographic preference of V1-V2, V1-V3, V1-V4, and V1-V5 pairs of the variants. This presumably implies that the martensitic transformation involved variant selection.

4. Discussion

As follows from the EBSD results considered above, it is likely that FSP exerted only a minor influence on the orientation relationship between the austenite and martensite but promoted the pronounced variant selection during martensitic transformation. The latter effect can be due to severe plastic strain in the austenitic phase field, which

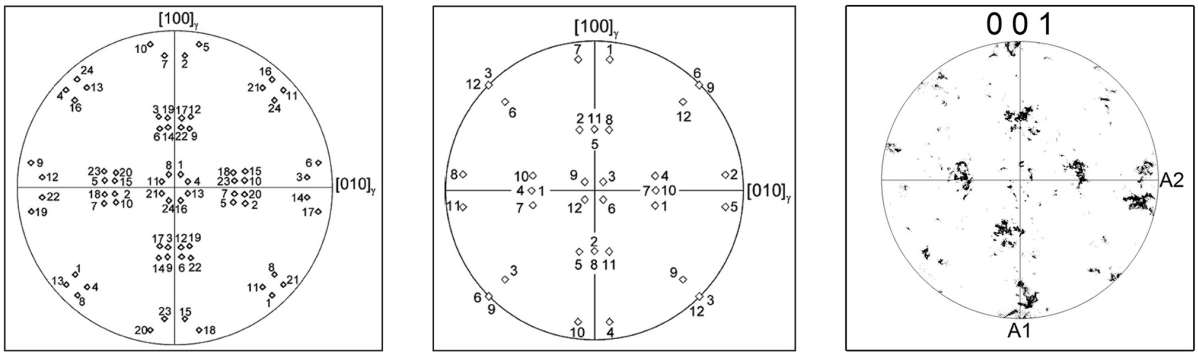

a b c

Fig. 4. The ideal 100 pole figures expected for the K-S OR (a) and N-W OR (b), [27, 28] and the typical measured 100 pole figure derived from a single prior-austenite grain (c). The numbers in (a) and (b) indicate martensite variants.

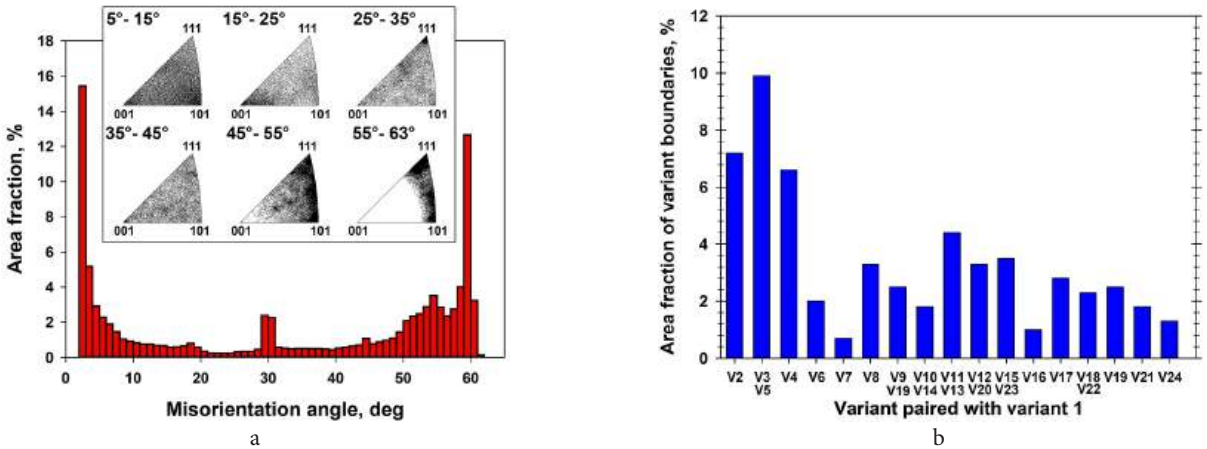

a b

Fig. 5. Misorientation distribution (a) and variant-pairing-frequency histogram derived from the martensitic phase (b). In the upper section of (a), the misorientation-axis distribution is shown as an inset.

promoted grain refinement and development of a distinct crystallographic texture. In order to examine this hypothesis, the prior-austenite grain structure was reconstructed.

The typical EBSD grain-boundary map taken from the stir zone is shown in Fig. 6 a. Assuming that the observed microstructure was produced during martensitic transformation, two different types of grain boundaries could be distinguished in the map [33]: (i) those existing in the prior-austenite structure (and thus outlining the prior-austenite grains) and (ii) those produced during martensitic transformation (i. e., the boundaries between the martensitic variants).

The misorientations between martensite variants can be easily calculated assuming either K-S, or N-W, or the mixed orientation relationship between the austenitic and martensitic phases [29]. These theoretical misorientations are summarized in the Table S3. Based on the specific misorientation, the intervariant boundaries can be easily discriminated from the prior-austenite boundaries in an EBSD map. This characteristic of the intervariant boundaries was used for the reconstruction of the prior-austenite grain structure.

Assuming that the martensitic transformation in the present study was governed by the K-S orientation relationship, appropriate grain boundaries were defined and then "removed" from the EBSD in Fig. 6 a. The resulting microstructure was shown in Fig. 6 b. As a result, the contours of the original austenite grains became visible, but the microstructural pattern was not obvious. This was presumably due to the significant orientation spread present within the prior-austenite grains (Fig. 4 c), according to which the relation between the austenite and martensite could be described in terms of both the K-S and N-W orientation relationships (Fig. 3 c).

Hence, in accordance with the discussion provided in Section 3, the "mixed" model of the orientation relationship was applied. Consequently, the intervariant boundaries expected for the "mixed" orientation relationship (Table S3) were removed from the EBSD map in Fig. 6 a. The produced

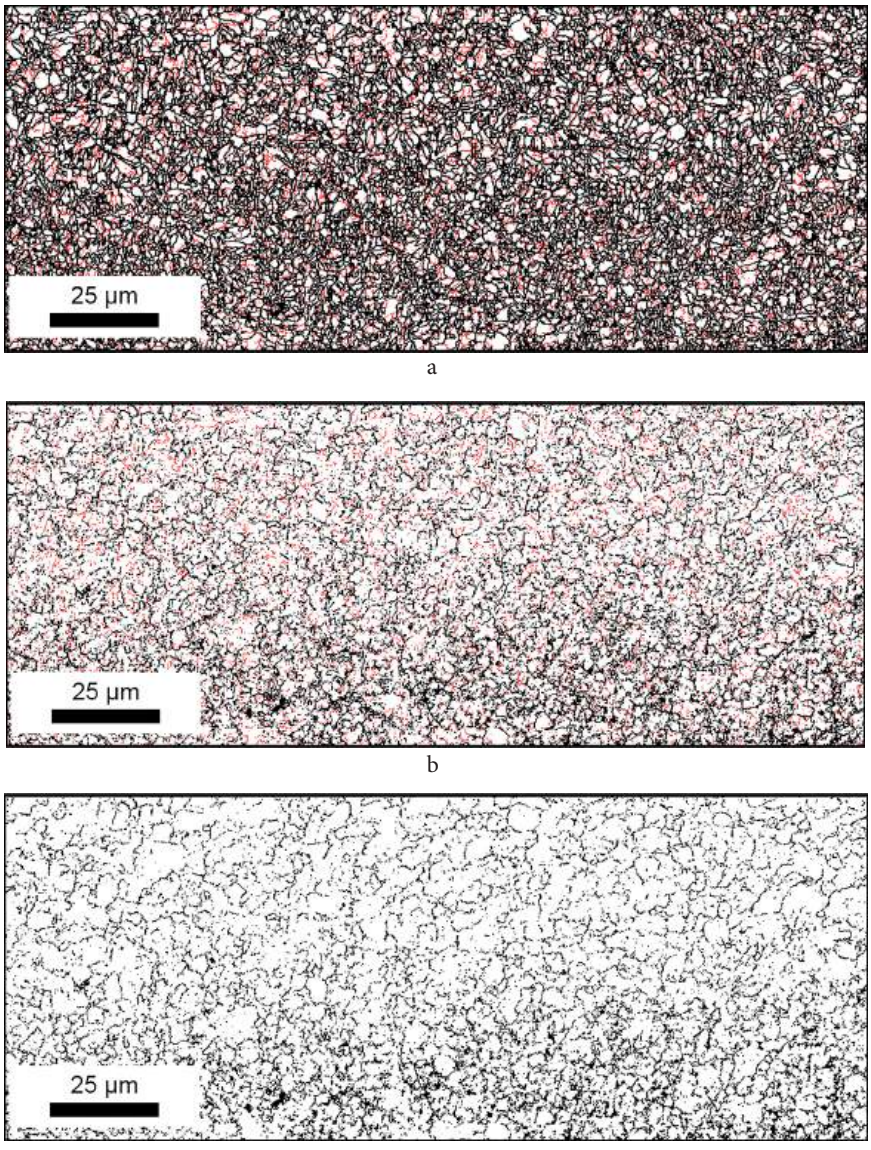

Fig. 6. (Color online) EBSD grain-boundary map of martensitic phase (a) and reconstruction of prior-austenite grain structure assuming the K-S orientation relationship (b) or mixed orientation relationship (c). In all cases, low angle boundaries (i. e., those with misorientation angle below 15°) are depicted as red lines, while high-angle boundaries (i. e., those with misorientation angle above 15°) are depicted as black lines.

microstructure was shown in Fig. 6c. The microstructural pattern became clearer, though some boundary traces of the prior-austenite grains were discontinuous in appearance. The latter observation was presumably attributable to the significant variability of the intervariant misorientations (Table S3). Due to the stochastic reasons, misorientations of some segments of the prior-austenite boundaries can be close to those of the intervariant boundaries and therefore were mistakenly removed from the EBSD map. Nevertheless, the contours of the reconstructed prior-austenite grains were seen enough to evaluate grain size. It was estimated to be about 10 μm, thus being essentially smaller than the prior-austenite grain size in the base material (35 μm). Therefore, FSP resulted in grain refinement in the austenitic phase, in broad agreement with expectations [34, 35].

Therefore, it was suggested that the variant selection revealed in the martensitic phase was associated with the grain refinement of the prior-austenite grain structure.

The black clusters in the bottom section of Fig. 6c are also worthy of remark. Those were the secondary particles, which presumably originated from the wear of the welding tool (Fig. 2). Remarkably, the prior-austenite grains in the vicinity of the tool debris are comparatively small (Fig. 6c). This suggests that the tool wear promotes an additional grain refinement effect, likely via the particle-stimulated-recrystallization mechanism.

Given the minor fraction of the retained austenite in the stir zone (≈0.1%), the reconstruction of the crystallographic texture produced in the austenitic phase during FSP is a challenging task. In the present study, the texture was evaluated on the basis of two assumptions.

First, it is commonly assumed that the straining mode during FSW/P is close to simple shear [36]. In face-centered cubic metals (including austenite), the simple shear textures are often examined using 111 and 110 pole figures [36], where the former pole figure shows the orientation of the closed-packed plane, while the latter one indicates the orientation of the closed-packed direction. Second, assuming the prevalence of the K-S relationship in the present study, {111} planes in austenite should be parallel to {110} planes in martensite, while <110> directions in the austenite should be parallel to the <111> directions in the martensite. Given the parallelism between the above planes and directions in the martensite and austenite, the 110 and 111 pole figures derived from the martensite can be used to examine the simple-shear texture in the austenite.

In accordance with the above discussion, the EBSD orientation data extracted from the martensitic phase were arranged as 110 and 111 pole figures (Fig. 7a) and then compared with the ideal simple-shear textures expected for the face-centered cubic crystals [36] (Fig. 7b). From the analysis, it was deduced that the crystallographic texture in the austenitic phase was close to the ideal B/-B {110}<112> simple-shear texture component. The formation of such a texture is often reported in FSW/Ped face-centered cubic metals (particularly, aluminum alloys).

Therefore, it was suggested that the variant selection occurred during martensitic transformation was contributed by the formation of the distinct crystallographic texture in the high-temperature austenite.

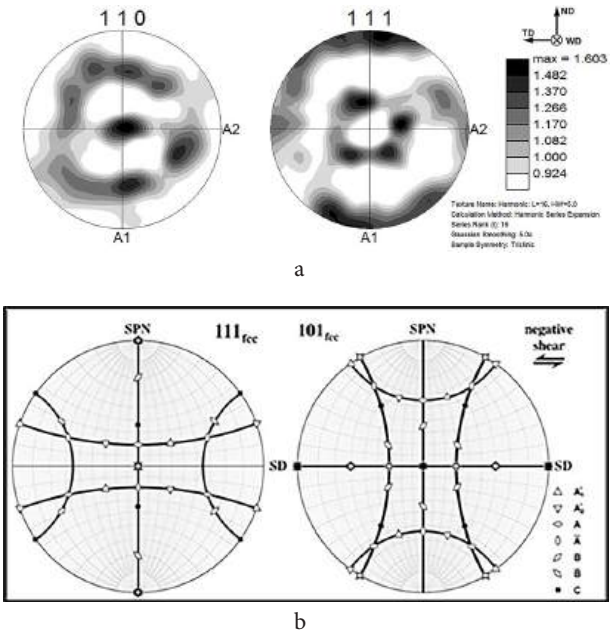

Fig. 7. 111 and 110 pole figures taken from of martensite (a) and the ideal simple-shear textures expected for face-centered cubic crystals (b) [36]. SD, SPN, WD, TD, and ND are shear direction, shear plane normal, welding direction, transverse direction, and normal direction, respectively.

5. Conclusions

In this work, crystallographic aspects of the martensitic transformation occurring during FSP of 10% Cr martensitic steel were examined. It was found that the orientation relationship between the martensite and the retained austenite somewhat deviated from the "classical" K-S relation. This observation was attributed to significant orientation spread within the prior-austenite grains produced during FSP. Moreover, it was also deduced that the martensitic transformation involved a pronounced selection of crystallographic variants. It was suggested that this phenomenon was associated with both the significant grain refinement and the formation of distinct crystallographic texture in the high-temperature austenite during FSP.

Supplementary material: *The online version of this paper contains supplementary material freely available at the journal's web site https://lettersonmaterials.com.*

References

1. J. Varghese, K.V. Rajulapati, K. Bhanu Sankara Rao, S.D. Meshram, G.M. Reddy, Ambient, elevated temperature tensile properties and origin of strengthening in friction stir welded 6 mm thick reduced activation ferritic-martensitic steel plates in as-welded and post-weld normalised conditions, Mater. Sci. Eng., A 857 (2022) 144019.
2. Y. Sun, H. Fujii, Y. Morisada, Double-sided friction stir welding of 40 mm thick low carbon steel plates using a pcBN rotating tool, J. Manuf. Processes 50 (2020) 319–328.
3. S. Zhu, X. Zhu, W. Lv, L. Cen, M. Gao, Y. Sun, L. Wu, H. Fujii, S. Guan, The influence of laser-induced tempering

on the microstructure and mechanical properties of 1500 MPa martensitic steel friction stir welded joints, Opt. Laser Technol. 182 (2025) 112094.
4. T. Hartman, M.P. Miles, S.-T. Hong, R. Steel, S. Kelly, Effect of PCBN tool grade on joint strength and tool life in friction stir spot welded DP 980 steel, Wear 328 – 329 (2015) 531 – 536.
5. Z. Wu, K. Ushioda, H. Liu, Y. Li, H. Fujii, Effect of V and Mn addition on the HAZ softening and tensile properties of friction stir welded martensitic steel, Mater. Sci. Eng., A 903 (2024) 146602.
6. M. Santella, Y. Hovanski, T.-Y. Pan, Friction Stir Spot Welding (FSSW) of Advanced High Strength Steel (AHSS), SAE Int. J. Mater. Manf. 5 (2012) 382 – 387.
7. S. Wang, X. Fan, X. Yang, Q. Zhang, K. Wu, D. Li, Feasibility of ZrC-W composite used as a tool of friction stir welding: First principles calculations and experiment, Ceram. Int. 44 (2018) 18650 – 18655.
8. S. Gain, S.K. Das, S.K. Acharyya, D. Sanyal, Friction stir welding of industrial grade AISI 316L and P91 steel pipes: A comparative investigation based on mechanical and metallurgical properties, International Journal of Pressure Vessels and Piping 201 (2023) 104865.
9. S. Gain, S. Kalyan Das, D. Sanyal, S. Kumar Acharyya, Exploring friction stir welding for joining 316L steel pipes for industrial applications: Mechanical and metallurgical characterization of the joint and analysis of failure, Eng. Fail. Anal. 150 (2023) 107331.
10. L. Pan, C.T. Kwok, K.H. Lo, Enhancement in hardness and corrosion resistance of AISI 420 martensitic stainless steel via friction stir processing, Surf. Coat. Technol. 357 (2019) 339 – 347.
11. S. Li, X. Yang, N. Vajragupta, W. Tang, A. Hartmaier, H. Li, The influence of post-weld tempering temperatures on microstructure and strength in the stir zone of friction stir welded reduced activation ferritic/martensitic steel, Mater. Sci. Eng., A 814 (2021) 141224.
12. M. Ragab, H. Liu, H.A. Abdel-Aleem, M.M. El-Sayed Seleman, M.M. Z. Ahmed, G. Mehboob, Numerical and experimental study of underwater friction stir welding of 1Cr11Ni2W2MoV heat-resistant stainless steel, J. Mater. Res. Technol. 29 (2024) 130 – 148.
13. G.M. Xie, R.H. Duan, P. Xue, Z.Y. Ma, H.L. Liu, Z.A. Luo, Microstructure and Mechanical Properties of X80 Pipeline Steel Joints by Friction Stir Welding Under Various Cooling Conditions, Acta Metall. Sin. (Engl. Lett.) 33 (2020) 88 – 102.
14. Y. Azuma, Y. Kaneno, T. Takasugi, Friction Stir Welding in Stainless Steel Sheet of Type 430 using Ni-base Dual Two-phase Intermetallic Alloy Tool, Quarterly Journal of the Japan Welding Society 28 (2010) 116 – 122.
15. P. Hua, S. Mironov, Y.S. Sato, H. Kokawa, S.H. C. Park, S. Hirano, Crystallography of Martensite in Friction-Stir-Welded 12Cr Heat-Resistant Steel, Metall. Mater. Trans. A 50 (2019) 3158 – 3163.
16. H.B. Zhang, Z.W. Wang, P. Xue, J.H. Li, W.G. Wang, H. Zhang, D.R. Ni, F.C. Liu, B.L. Xiao, Z.Y. Ma, Eliminating heat-affected zone of nuclear heat-resistant steel joint via low-temperature friction stir welding, Mater. Sci. Eng., A 916 (2024) 147340.
17. M. Ragab, H. Liu, M.M. Z. Ahmed, G.-J. Yang, Z.-J. Lou, G. Mehboob, Microstructure evolution during friction stir welding of 1Cr11Ni2W2MoV martensitic stainless steel at different tool rotation rates, Mater. Charact. 182 (2021) 111561.
18. G.M. Xie, R.H. Duan, Y.Q. Wang, Z.A. Luo, C. Wang, G.D. Wang, Crystallography of the nugget zone of bainitic steel by friction stir welding in various cooling mediums, Mater. Charact. 182 (2021) 111523.
19. S. Rahimi, B.P. Wynne, T.N. Baker, Development of Microstructure and Crystallographic Texture in a Double-Sided Friction Stir Welded Microalloyed Steel, Metall. Mater. Trans. A 48 (2017) 362 – 378.
20. A. Falekari, H.R. Jafarian, A.R. Eivani, M. Habibnejad-korayem, A. Heidarzadeh, Friction stir processing of thick tempered martensitic steels: Correlation between microstructure and mechanical properties, Mater. Sci. Eng., A 836 (2022) 142698.
21. P. Xue, B.L. Xiao, W.G. Wang, Q. Zhang, D. Wang, Q.Z. Wang, Z.Y. Ma, Achieving ultrafine dual-phase structure with superior mechanical property in friction stir processed plain low carbon steel, Mater. Sci. Eng., A 575 (2013) 30 – 34.
22. P. Xue, W.D. Li, D. Wang, W.G. Wang, B.L. Xiao, Z.Y. Ma, Enhanced mechanical properties of medium carbon steel casting via friction stir processing and subsequent annealing, Mater. Sci. Eng., A 670 (2016) 153 – 158.
23. L. Huang, K. Wang, W. Wang, K. Zhao, J. Yuan, Q. Wang, K. Qiao, J. Cai, Corrosion properties of low carbon steel prepared by submerged friction stir processing, Mater. Corros. 69 (2018) 1077 – 1083.
24. H. Das, K.-J. Lee, S.-T. Hong, Study on Microtexture and Martensite Formation of Friction Stir Lap-welded DP 590 Steel within A_1 to A_3 Temperature Range, J. Mater. Eng. Perform. 26 (2017) 3607 – 3613.
25. H. Ashrafi, M. Shamanian, R. Emadi, M. Ahl Sarmadi, Comparison of Microstructure and Tensile Properties of Dual Phase Steel Welded Using Friction Stir Welding and Gas Tungsten Arc Welding, Steel Res. Int. 89 (2018) 1700427.
26. S. Li, N. Vajragupta, A. Biswas, W. Tang, H. Wang, A. Kostka, X. Yang, A. Hartmaier, Effect of microstructure heterogeneity on the mechanical properties of friction stir welded reduced activation ferritic/martensitic steel, Scripta Mater. 207 (2022) 114306.
27. Y.S. Sato, H. Kokawa, H.T. Fujii, Y. Yano, Y. Sekio, Mechanical Properties and Microstructure of Dissimilar Friction Stir Welds of 11Cr-Ferritic/Martensitic Steel to 316 Stainless Steel, Metall. Mater. Trans. A 46 (2015) 5789 – 5800.
28. Y. Yano, Y.S. Sato, Y. Sekio, S. Ohtsuka, T. Kaito, R. Ogawa, H. Kokawa, Mechanical properties of friction stir welded 11Cr-ferritic/martensitic steel, J. Nucl. Mater. 442 (2013) S524 – S528.
29. B. Sonderegger, S. Mitsche, H. Cerjak, Martensite laths in creep resistant martensitic 9 –12% Cr steels — Calculation and measurement of misorientations, Mater. Charact. 58 (2007) 874 – 882.
30. A. Mirzaei, C.D. Barrett, X. Ma, P.D. Hodgson, H. Beladi,

On the propensity of lath martensite intervariant boundaries to hydrogen absorption using molecular statics simulation, Mater. 25 (2022) 101539.
31. A. Mirzaei, P. D. Hodgson, X. Ma, V. K. Peterson, E. Farabi, G. S. Rohrer, H. Beladi, The role of parent austenite grain size on the variant selection and intervariant boundary network in a lath martensitic steel, Mater. Sci. Eng., A 889 (2024) 145793.
32. A. Stormvinter, G. Miyamoto, T. Furuhara, P. Hedström, A. Borgenstam, Effect of carbon content on variant pairing of martensite in Fe-C alloys, Acta Mater. 60 (2012) 7265 – 7274.
33. N. Gey, M. Humbert, Characterization of the variant selection occurring during the α→β→α phase transformations of a cold rolled titanium sheet, Acta Mater. 50 (2002) 277 – 287.
34. C. Cheng, K. Kadoi, H. Fujii, K. Ushioda, H. Inoue, Improved strength and ductility balance of medium-carbon steel with chromium and titanium fabricated by friction stir welding process, Mater. Sci. Eng., A 803 (2021) 140689.
35. Z. Wu, T. Nagira, K. Ushioda, G. Miyamoto, H. Fujii, Microstructures and tensile properties of friction stir welded 0.2%C -Si-Mn steel, Mater. Sci. Eng., A 799 (2021) 140068.
36. R. W. Fonda, K. E. Knipling, Texture development in friction stir welds, Sci. Technol. Weld. Joining 16 (2011) 288 – 294.